PHYSICAL REVIEW ACCELERATORS AND BEAMS **27,** 073501 (2024)

Laser-driven acceleration of a 94.8 MeV uniform proton beam enhanced by a thin axial absorber rod

Husam Y. Al-Omari,[1,*] Mohamed E. Yahia,[1,†,§] and Ali M. Almomani[2,‡,§]
[1]*Abu Dhabi Polytechnic, Institute of Applied Technology, Abu Dhabi 111499, United Arab Emirates*
[2]*Physics Department, Yarmouk University, Irbid 21163, Jordan*

(Received 20 January 2024; accepted 1 July 2024; published 22 July 2024)

Laser-based proton accelerators offer promising advantages for many sensitive applications due to their compact size. However, achieving uniform beams with a narrow energy spread remains a challenge. Here, a beamline simulation is performed using the TraceWin and SRIM codes to optimize the spectral and spatial characteristics of a laser-driven proton beam. This beamline, comprised of four magnetic quadrupoles and equipped with a thin axial absorber rod in conjunction with an energy selection aperture for narrowing the energy spread, a carbon scatterer foil for beam spot smoothing, and an angular selection aperture for beam collimation, effectively transports a selected proton beam energy within the range of 50–250 MeV. In this work, laser-accelerated protons with a wide energy spread were transported through the proposed beamline, which was optimized for 109 MeV protons. The protons emerged well-collimated with a significantly narrowed energy spread of 94.8 ± 3.9 MeV (a reduction from the intended 109 MeV due to passage through the scatterer) and a homogenized, 11 mm diameter beam spot while maintaining a transmission efficiency above 2.2%.

DOI: 10.1103/PhysRevAccelBeams.27.073501

I. INTRODUCTION

Laser-based proton accelerators, one of the laser-plasma accelerators, have seen many advancements since their establishment [1,2]. The high gradient electric field (tens to hundreds of TV/m) in the laser accelerator enables the generation of intense and energetic proton bunches [3–5] with a subpicosecond duration [6]. The laser-based proton accelerators exhibit distinct characteristics, making them promising compact sources with potential applications in many fields [7–10].

Since the generation of the first petawatt laser pulse in 1996 [11], various petawatt laser facilities were established, dedicated to researching applications in various fields like isochoric heating of matter [12], fast ignition of fusion targets [13], radiography [14–16], medical applications [5,9,10,17–21], materials science [6], and astrophysics [22–25].

In laser-plasma interaction, several acceleration mechanisms were proposed to describe the laser-driven acceleration. These mechanisms were subjected to laser and target configurations. In general, the laser intensity and pulse duration with target thickness are the key factors in the acceleration mechanism. Target normal sheath acceleration (TNSA) was the most extensively studied mechanism and applied to relatively thick targets (~µm). The energy spectrum of accelerated protons in TNSA is a quasiexponential profile with a maximum recorded cutoff energy of 85 MeV [26]. Later, advance in laser technology and target preparation boosted the acceleration to levels beyond the TNSA. Several acceleration mechanisms emerged in parallel by using ultrashort laser pulses (tens to hundreds fs) with intensities exceeding $10^{20}\ \mathrm{W/cm^2}$ on ultrathin (~nm) targets [27]. The most popular acceleration mechanisms that emerged were radiation pressure acceleration in the light sail (RPA-LS), radiation pressure acceleration in the hole-boring (RPA-HB), and break-out afterburner (BOA) ion acceleration [25,28].

The TNSA and later advanced mechanisms utilize electrons as a mediator to transfer energy from the laser to ions [29,30]. The advanced mechanisms (RPA-LS, RPA-HB, and BOA) differ in pulse duration and target thickness [27]. In RPA, the generated plasma must remain over dense during the interaction with a laser pulse. This requires using a laser pulse duration ranging from 30 to 50 fs [27]. If the target is thin enough, the ions will accelerate continuously as a light sail regime and the RPA-LS mechanism will be the case [31]. In thicker targets, the RPA-HB mechanism is more feasible where the laser pulse penetrates deeply as in the hole-boring (HB) regime [27,31] and reaches the rear side before the laser pulse ends [27]. In BOA, the duration of the incident laser pulse exceeds tens of fs time scale to a

---

[*] Contact author: omarihusam@hotmail.com
[†] Contact author: mohamed.kelib@actvet.gov.ae
[‡] Contact author: ali.almomani@yu.edu.jo
[§] These authors contributed equally to this work.

few hundred fs, in which the over dense constraint will not be achieved [27].

In general, achieving specific beam qualities is essential when employing laser-driven protons in various applications. These qualities encompass controlled spectral and spatial shapes, particle number, satisfactory reproducibility, and stability. In certain applications, such as particle therapy, accessing higher energy ranges and achieving high repetition rates (multiple proton bunches per second) are essential. In a recent experimental study, researchers investigated an innovative approach by employing a cooled hydrogen jet plasma as a laser target [32,33]. They achieved remarkable results with recorded energies reaching up to 80 MeV. The technique used in this study has the potential to generate multiple proton bunches per second [33]. Another study [2] adopted a hybrid acceleration scheme that incorporated RPA-TNSA mechanisms. In this investigation, accelerated protons exceeding 94 MeV were recorded using an ultrathin foil irradiated by a linearly polarized laser pulse.

However, the laser-driven protons produced in the aforementioned laser acceleration mechanisms have drawbacks that limit their application. These drawbacks pertain to beam quality issues, such as a wide energy spread and large opening angle. Several studies have concentrated on optimizing beamlines that incorporate magnetic elements, offering both focusing and energy selection capabilities, to collect and transport laser-driven protons for various applications [5,9,19,21,34–40]. Most of these studies were limited to proton energies ranging from a few to tens of MeV. Notably, two studies, [5] and [21], utilized a single solenoid to focus a reference energy of 200 MeV. In the [21] study, the solenoid was supported with an energy selection aperture and a scatterer. The aim was to transport homogenized protons within a ±36.5% energy window centered around 200 MeV. A study ([41]) compared the transportation efficiency of solenoids and quadrupoles for proton energies ranging from a few to hundreds of MeV. This study demonstrates that quadrupoles offer a convenient solution for handling higher energy levels as the field strength stays within the iron saturation. In this study, we present the design and optimization of a compact laser-accelerated proton beamline, incorporating four magnetic quadrupoles and employing techniques to narrow and smooth the energy band around 94.8 MeV of the laser-accelerated proton beam. The simulation of beam dynamics through the energy selection system, utilizing 6D RPA protons, is conducted using the TraceWin and SRIM codes [18,30,36,42–44].

II. LASER-ACCELERATED PROTON BEAMLINE

A. Physics of the beamline setup

1. Layout scheme (Fig. 1)

The wide energy spread and large opening angle of ion and proton beams, generated using lasers, pose significant challenges in their utilization across various applications. These factors are widely acknowledged as key limitations in the integration of laser-driven protons across diverse applications. Therefore, a suggested optimal scheme should combine focusing with energy selection in the beam line. Many studies have used a conventional dispersive technique with laser-accelerated protons, for energy selection [20,45–48]. The laser-driven protons demonstrate a broad transverse divergence angle [21,49]. Consequently, protons of different energies will spatially mix once they pass through the magnetic field of the dipole [45]. To achieve effective proton spatial differentiation, the dispersion process is preceded by a collimation system. Collimation can be achieved using two beamline configurations: one involves a primary collimation device with a small opening angle, which poses a shielding challenge as it generates secondary neutrons and photons due to the protons stopping in the collimation device [45], thereby resulting in significant efficiency loss [41,45]. Alternatively, as observed in recent studies, collimation has been achieved using magnetic elements, such as solenoids [20,46,48] or quadrupoles [47]. In both beamline dispersive configurations, the bending element is followed by magnetic arrangements to cancel the spatial dispersion in energy [20] and reshape the filtered beam to the desired beam profile size [20,46]. However, this approach might introduce complexities in beamline design and matching, as noted in previous studies [20,46,48]. Alternatively, the chromatic effect of solenoid and quadrupole magnets combines transverse focusing with energy selection. Therefore, utilizing them instead of beamline dispersive configurations will simplify beamline design and matching, making it more compact. The high energy ranges employed in certain applications boost the use of multiple quadrupoles beyond a solenoid, as the field strength stays within the iron saturation [41]. Three quadrupoles or more are preferred for smoother focusing compared to doublet [41].

In this paper, a beamline of four quadrupoles and an aperture has been proposed for focusing and energy selection. Initially, the beamline was designed to bring monoenergetic protons with an energy of 109 MeV, an initial source radius of 25 μm, and a divergence of ±60 mrad, to a focal point at 2 m. TraceWin code [42] was used for the beam matching calculations. A standard Kapchinsky-Vladimirsky transverse ellipsoid, centered at the reference energy (109 MeV), was implemented in TraceWin for this purpose. Later, to select a ±3% energy spread from a wider energy spectrum, an energy selection aperture with a diameter of 3 mm was placed at the 2 m focal point. Figure 2 shows the beam envelope evolution along the z axis for 109 MeV monoenergetic protons. The geometrical parameters and matching results are summarized in Table I.

The same beamline, equipped with movable elements (flexible drifts) and utilizing varied PMQs strengths (pulsed magnetic quadrupoles), can transmit selected proton beams ranging from 50 to 250 MeV while constraining the output

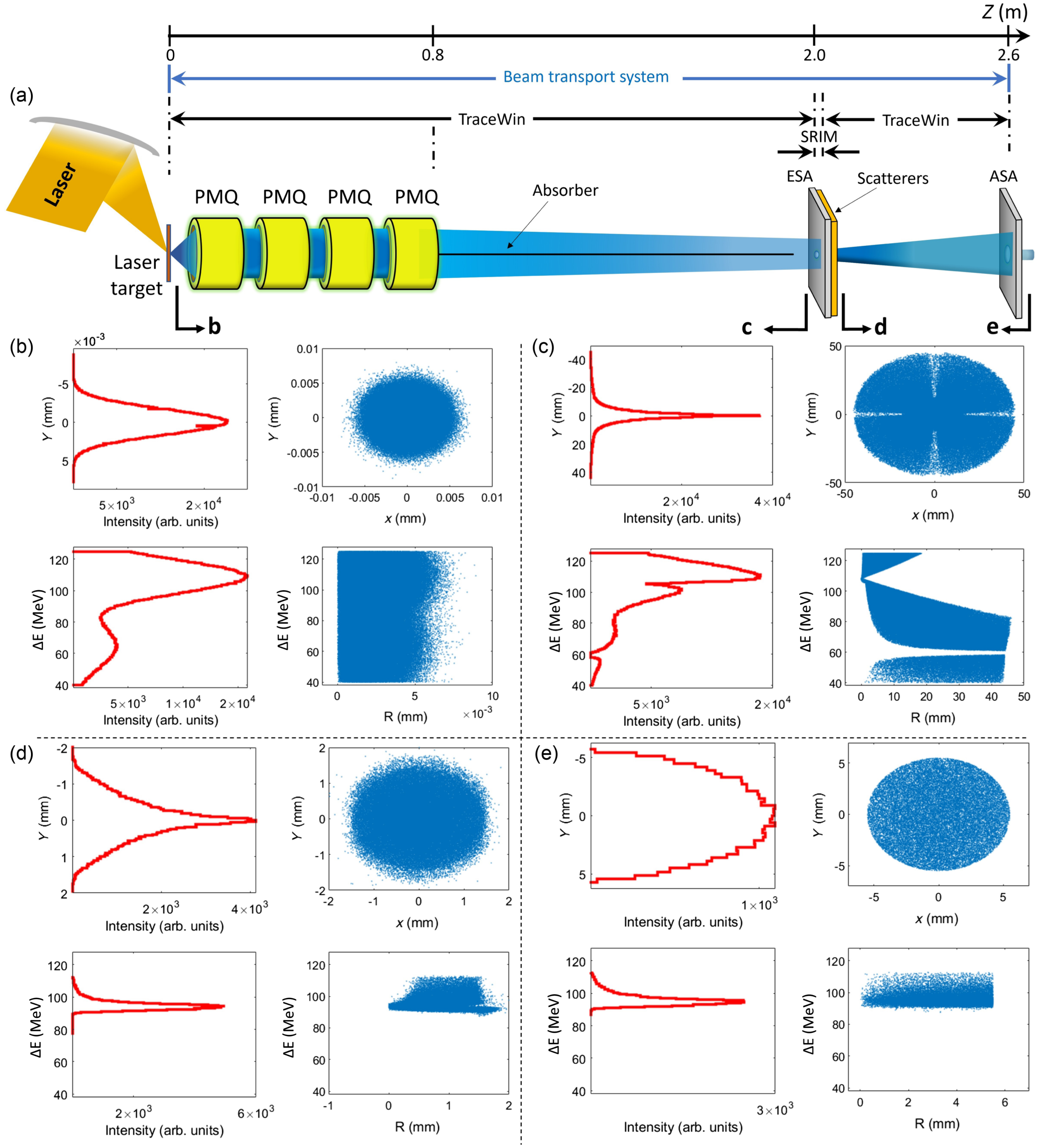

FIG. 1. An overview of the beam transport system. (a) Broadband generation of laser-accelerated protons driven by a focused ultrashort high-intensity laser pulse impinging on the laser target. A selected energy band of protons is transported through a beamline utilizing four pulsed magnetic quadrupoles (PMQs). A thin cylindrical absorber rod is positioned along the axial axis before the energy selection aperture (ESA) to truncate low-energy protons. The ESA is inserted for spectral shaping and scatterer for lateral homogenization. The angular selection aperture (ASA) is inserted for beam collimation. The protons traverse the ASA downstream the proposed beamline. Comparing the transverse beam profile and energy spectrum distributions: (b) input, (c), (d) before and after ESA (output of the SRIM simulation), (e) output. Density profiles are highlighted in red.

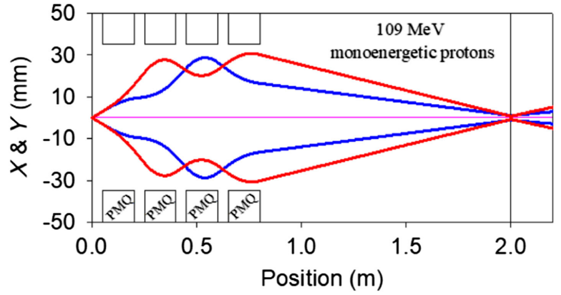

FIG. 2. Beam envelope evolution along the z axis for monoenergetic protons with an initial energy of 109 MeV and a divergence of ±60 mrad. The blue line represents the x direction, while the red line represents the y direction.

beam's energy spread to ±3%. These parameters can be calculated using TraceWin's beam-matching feature. Figure 3 illustrates the evolution of the beam envelope along the z axis for protons with energies of 50, 170, and 250 MeV, with the beam's energy spread constrained within ±3% and a divergence of ±60 mrad. Here, the focal spot for selected beam energies is matched at the energy selection aperture (ESA) using varied pulsed quadrupole strengths while maintaining the same drift distances (shown in Table I).

2. Initial beam distribution

The generated proton distribution was fitted close to the output of the RPA simulation presented in [5]. The distribution was scaled in the energy spectrum and used as input for our study. The energy spectrum presented in [5] (Fig. 4) exhibits a pronounced peak at 220 MeV with a standard deviation of around 20 MeV. Additionally, the spectrum displays a relatively broad foot extending toward lower energies. Notably, the energy spectrum of laser-driven protons demonstrates a relatively weak dependence on the transverse divergence angle (±Ω). The simulated energy spectrum was approximated using a bi-Gaussian function, shown as a continuous red solid line in Fig. 4 [21]. The pronounced peak in the scaled energy spectrum (Fig. 5, left) was reduced to approximately half of its original value (109 MeV) to align more closely with the energy ranges recently attained in experimental studies [2,32,33]. The standard deviation of the apparent peak was also reduced accordingly. The broad foot at low energies is supposed to peak at 65 MeV with a standard deviation of 35 MeV.

TABLE I. Geometrical parameters of a beamline for focusing 109 MeV protons at 2 m. PMQ stands for pulsed magnetic quadrupole.

Element	Length (mm)	Radius (mm)	Field (T/m)	Polarity
Drift	50	50		
PMQ1	150	35	72.1	xz plane
Drift	50	50		
PMQ2	150	35	74.5	yz plane
Drift	50	50		
PMQ3	150	35	69.0	xz plane
Drift	50	50		
PMQ4	150	35	34.0	yz plane

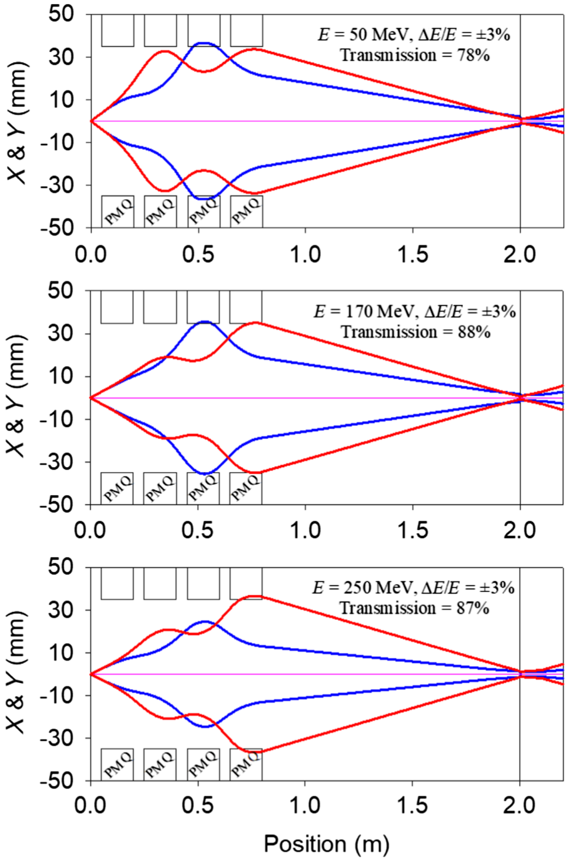

FIG. 3. Beam envelope evolution along the z axis for 50, 170, and 250 MeV protons. The beam's energy spreads are limited to ±3% and divergences of ±60 mrad. The percentage of transmitted particles (source-to-end) is shown for all selected beam energies. The blue line represents the x direction, while the red line represents the y direction.

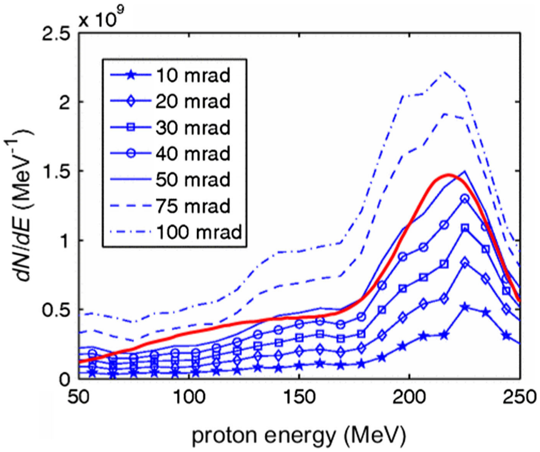

FIG. 4. Simulated energy spectrums for different capture cone angles Ω with the bi-Gaussian fit in red.

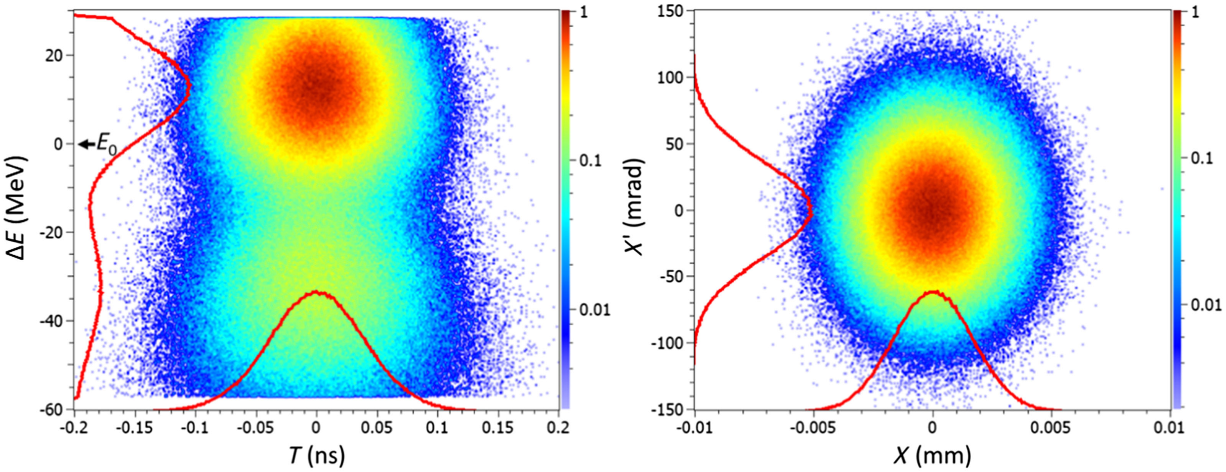

FIG. 5. Initial phase space distributions with density profiles in red. The standard deviations for the variables x, x', and t are, respectively, 1.25 μm, 25 mrad, and 30 ps. The standard deviations for the 109 and 65 MeV energy peaks were 10 and 35 MeV, respectively. In TraceWin code, the energy in phase spaces is represented relative to an average beam energy ($E_0 = 97$ MeV). The colorbar represents the relative density, rescaled for each plot.

Furthermore, we have arbitrarily set the lower energy cutoff at 40 MeV. This decision stems from the fact that protons with energies below 40 MeV will not contribute to the output beam. The generated beam distribution uses 10^6 particles and randomly Gaussian distributed in phase space and time domain. The chosen rms values in phase space were 1.75 μm and 35 mrad, while it was 42 ps in pulse duration (Fig. 5).

3. Space-charge effect

In the early stages, when we are close to the source target, there is a dense concentration of protons that expand over a short period of time. During this expansion, the electric charge created by these protons is essentially balanced out by the presence of electrons that are comoving with them. This balancing of charges is described as "neutralization" [34,50]. However, as we move away from the source and approach the fringe field of the first pulsed magnetic quadrupole (PMQ), something changes. In this region, the motion of both protons and the accompanying electrons is influenced by the differences in their masses and charges. As a result, the previously achieved neutralization begins to break down, and the interaction between the protons and electrons becomes more complex. This breakdown of neutralization starts to dominate the behavior of the particles in the fringe field of the PMQ.

The space charge is inversely proportional to proton energy and diminishes with the temporal expansion up to the PMQ aperture. This is because higher energy protons are less affected by electrostatic repulsion and can maintain a more compact beam. A previous study [30] found that a quadrupole, which was placed 70 mm away from a source, maintained its focusing efficiency for a particular energy range (9 ± 0.5 MeV), even when there was space-charge repulsion present. This was for a focused energy 12 times lower than this study. Therefore, the higher energy ranges used in this study weaken the space-charge effect further. This is beside the temporal expansion in the drift preceding the PMQ aperture and neutralization up to the PMQ fringe field. The charge separation in the PMQ fringe field causes a space-charge repulsion, resulting in both transverse and longitudinal expansion. The transverse expansion ultimately reduces the transmission through the selection aperture at 2 m. For simplicity, we assumed that the full space-charge effect begins at a distance of 10 mm before the PMQ, which is located 50 mm from the source. The transmission of a proton beam, weighted to a total intensity of 10^{10} protons (≈173 mA), through the entire system (source-to-end), and past the energy selection aperture (ESA, 3 mm diameter, located at 2 m) was evaluated using TraceWin. The transmission decreased marginally from 17.94% to 17.85%, indicating a loss of 0.09%. Thus the space-charge effect, in this case, is very weak and can be ignored.

B. Optimization of a proton beam

Protons (with a bi-Gaussian energy distribution shown in Fig. 5) tracked through the proposed scheme, consisting of four quadrupoles and an energy selection aperture at 2 m, exit the scheme with a non-negligible broadening of the energy spectrum tails. This is accompanied by nonhomogeneity in the transverse beam profile due to the correlation between focused energy and transverse position (radial-energy correlation). The resulting distribution at 2 m after the energy selection aperture is shown in Fig. 6. The nonhomogeneity can be clearly observed. Therefore, from a practical standpoint, it is beneficial to filter the energy spectrum using a filtering tool and then smooth the beam

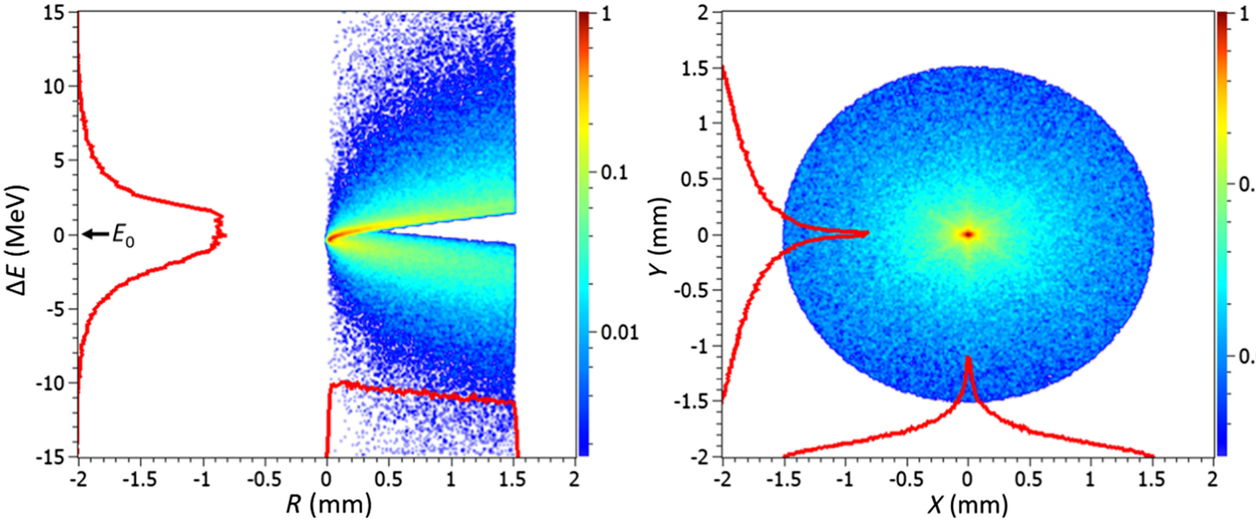

FIG. 6. Radial-energy correlation and transverse beam profile after the energy selection aperture of 3 mm diameter at 2 m. TraceWin represents the energy in phase space, adjusted relative to the average energy of all protons ($E_0 = 108$ MeV). The colorbar represents the relative density, rescaled for each plot. Density profiles are highlighted in red.

through the radial energy beam profile using a suitable scatterer.

1. *Energy tails suppression*

The wide-energy-tails pose challenges for targeting a confined target in a medium, such as in proton therapy. Therefore, a truncation of the energy tails must be applied to the energy spectrum. This has to be done to enhance targeting precision and improve confinement. In the case of proton therapy application, utilizing a proton beam with a nonconfined energy spectrum may result in an undesirable dosage received by lower and distal depths. The dose profile delivered to nontargeted tissues at lower depths is primarily influenced by the lower energy tail. These depths receive a smaller portion of the dose from higher energy protons. On the other hand, the higher energy tail extends beyond the targeted tissue and deposits its energy in distal healthy tissues.

To achieve additional energy filtration in lower energies along the axis before the energy selection aperture, a thin axial absorber rod can be utilized. The higher energies, which are concentrated near the aperture, can also be filtered by placing an additional thin axial absorber rod after the energy selection aperture. This filtration technique was originally proposed by Hofmann *et al.* [21]. However, it is important to note that in our work, the absorber rod is primarily limited to filtering lower energies, while the selection aperture adequately filters protons with higher energies.

Beyond the energy selection aperture (as shown in Fig. 6), the energy spectrum is broad due to the transmission of off-energies. Prior to the energy selection aperture, the lower energy protons are focused along the axial axis. To address this, a rod of tungsten, as mentioned in [21], with a small diameter (approximately 1 mm) can be placed along the axial axis before the energy selection aperture. Using ATIMA [51], the stopping depth for 130 MeV protons is approximately 1.4 cm. This absorber effectively filters out the lower energy protons, as well as the higher energy protons that are close to the axis.

In the TraceWin code, this implementation can be achieved using a series of coaxial ring apertures. The sequence of apertures spans from 80 to 190 cm and includes an inner cylindrical absorber with a radius of 0.5 mm, along with an outer coaxial radius of 40 mm. In beam tracking, particles that collide with the internal beam pipes, absorber (ring apertures), or aperture edges are simply frozen and excluded from the TraceWin beam tracking simulation. Consequently, the scattering and secondary particles within the beamline setup are not treated. Shielding the beamline against secondary particles is discussed in some detail in Ref. [45] for a similar beamline with bending magnets. The handling of scattered and secondary particles that may pass through the angular selection aperture (ASA) is left to future work. For visual reference, Fig. 7 presents a radial density plot from the source up to 10 cm after the energy selection aperture. The geometry of the ring aperture sequence ensures the filtration of particle energies below 105 MeV, which move with minimal radial extent along the axial axis. The green color in the supposed absorber rod region indicates a low density of protons. This is due to the fact that in the TraceWin code, the coaxial ring apertures were separated by 1 cm drifts. Consequently, the lower-energy protons are focused and can access these drifts, becoming trapped at the inner coaxial radius. The truncation of lower energy protons, which move close to the axis, is evident in the radial energy profile shown in Fig. 8, when compared to Fig. 6 (left).

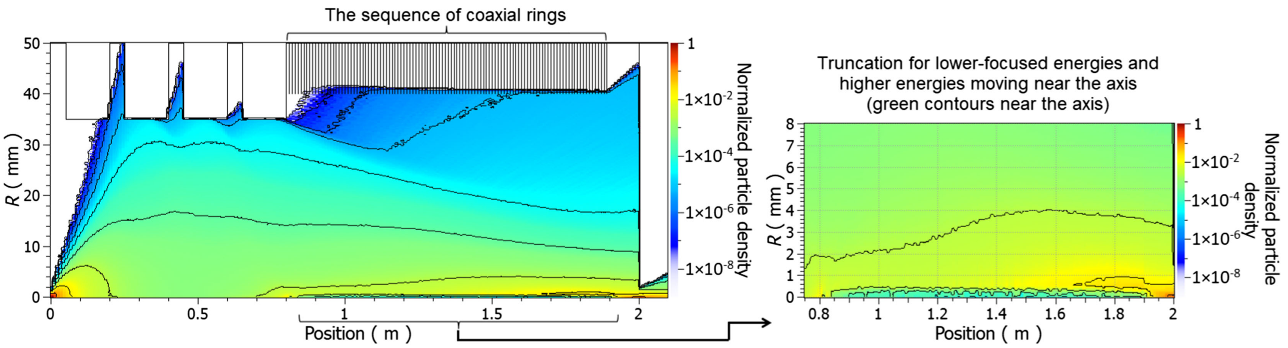

FIG. 7. Left: radial density plot extends from the source up to 10 cm after the energy selection aperture. Additionally, there are a series of coaxial apertures with inner radii of 0.5 mm located between 80 and 190 cm from the laser source. The contours on the plot indicate constant density levels. Right: this is a zoomed-in view of the region between 80 and 190 cm, which shows the truncation of protons with lower-focused energies and higher energies moving near the axis. The colorbar represents the relative density.

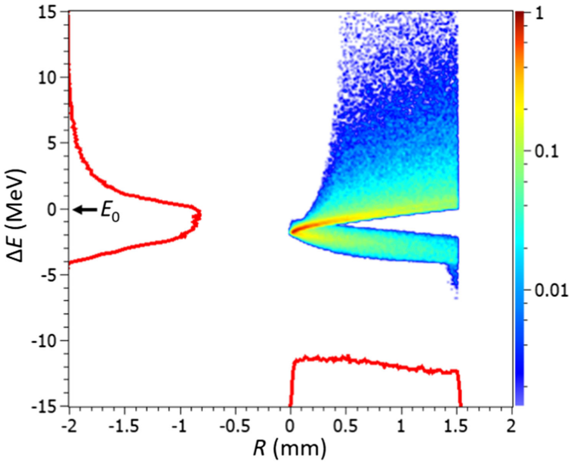

FIG. 8. Radial-energy profile with the sequence of ring apertures after the energy selection aperture at 2 m. The energy in phase space is represented relative to an average beam energy of $E_0 = 109.5$ MeV. The colorbar represents the relative density. Density profiles are highlighted in red.

2. Radial-energy decorrelation in beam profile

The radial-energy correlation appears as a steep imprint in density of transverse beam profile, presenting an inconsistency with the required homogeneity in certain applications (Fig. 6). The correlation is mainly caused by the chromaticity, where different energies are focused at different axial positions. Thus the focused energy is concentrated in the beam center compared with the in focused and defocused energies.

A decorrelation in the radial-energy profile can be achieved by using a scattering target, which induces transverse angular straggling. This straggling in the transverse angular direction reproduces the central transverse density and ultimately results in effective smoothing of the steepness of the central transverse density. The thickness of the scattering target is crucial for beam quality, specifically regarding energy loss and transmission through an angular selection aperture located at 2.6 m, which acts as a collimator for the transmitted beam. Therefore, the thickness of the scattering target should be carefully balanced to

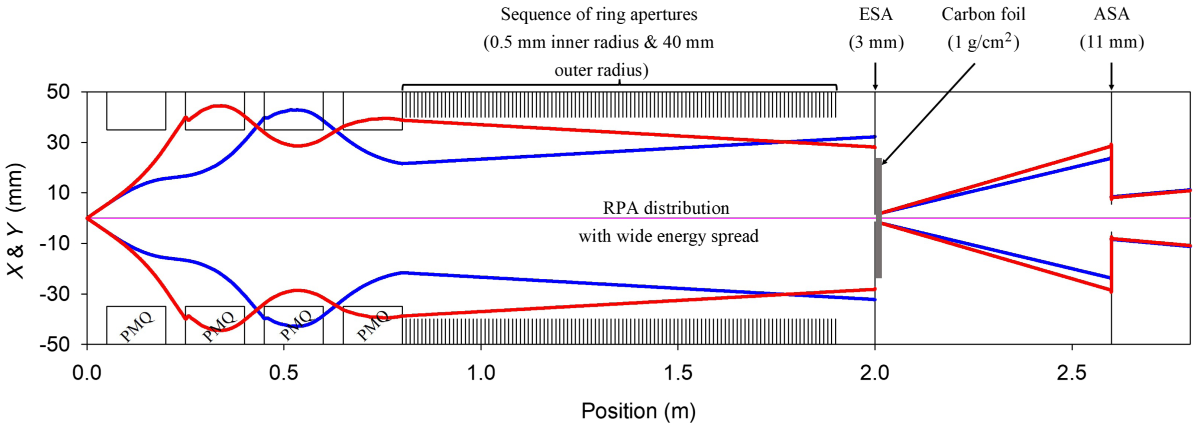

FIG. 9. Beam envelope evolution along the z axis for the RPA distribution with wide energy spread. The plot shows the four quadrupoles, a sequence of ring apertures, energy, and angular selection apertures. The carbon scatterer foil is highlighted to show its position in the beamline layout. The blue line represents the x direction, while the red line represents the y direction.

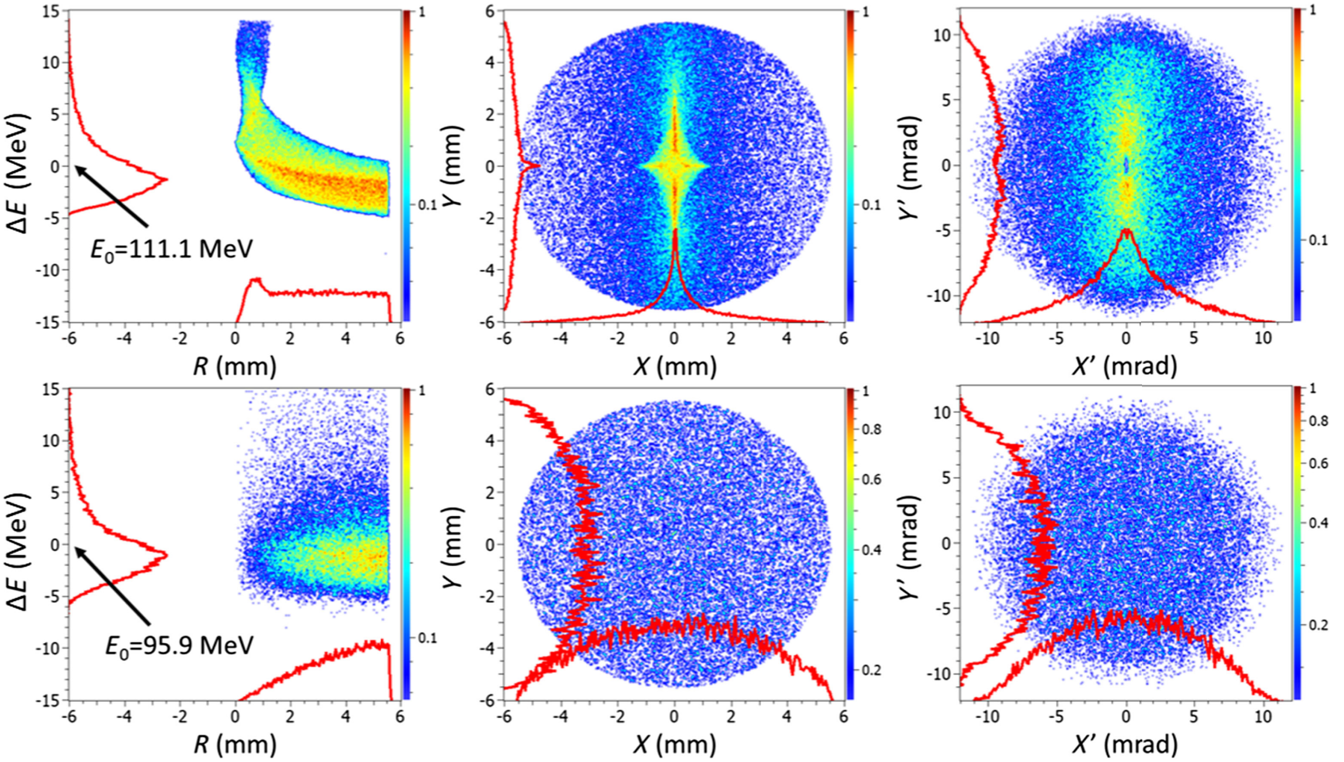

FIG. 10. Resulting distributions at 2.6 m after the angular selection aperture without (top) and with (bottom) carbon foil. Transmission is reduced from 6.1% in the absence of a carbon foil to 2.2% in the presence of a carbon foil. This figure represents the average beam energy, E_0, for both cases. The colorbar represents the relative density, rescaled for each plot. Density profiles are highlighted in red.

achieve effective smoothing with minimal energy loss and satisfactory transmission.

In a previous study, three scatterers were positioned between a pulsed magnetic solenoid and the energy selection aperture [21]. In this context, we propose the utilization of a $1\ \mathrm{g/cm^2}$ carbon scatterer foil placed at 2 m from the source directly behind the energy selection aperture.

By utilizing the ATIMA code [51], a simulated 109 MeV proton beam, parallel to the beam axis, exits the foil with an angular straggling of 10.6 mrad and an energy loss of 5.6%. The beam dynamics simulation for the bi-Gaussian proton energy distribution (shown in Fig. 5) was performed from the laser-target down to the end of the channel using the TraceWin code. The SRIM code [43] was employed to transport the proton distribution through the carbon foil. The envelope plots, which include a four-quadrupole scheme, a sequence of ring apertures, energy, and angular selection apertures, are shown in Fig. 9.

Figure 10 displays the resulting distributions at 2.6 m from the source directly behind the angular selection aperture without (top) and with (bottom) the carbon foil. It can be observed that the carbon foil successfully resolves the radial-energy correlation and removes the tendency of higher energies to concentrate close to the axis. Furthermore, the transmitted protons are almost collimated, with an rms divergence of 4.7 mrad, as shown in the angular phase profile (Fig. 10, bottom right). However, the expansion in the transverse beam profile reduces the transmission (source end) through the angular selection aperture from 6.1% to 2.2%.

III. CONCLUSIONS

Our work demonstrates the effectiveness of a novel beamline configuration for optimizing laser-accelerated protons, paving the way for their application in proton therapy and other possible applications. This beamline configured with four magnetic quadrupoles and supported by a thin axial absorber rod, an energy selection aperture, a carbon scatterer foil, and an angular selection aperture, effectively transports a selected proton beam energy within the range of 50–250 MeV. Our proposed beamline offers a compact and cost-effective alternative to the conventional ion source, radiofrequency quadrupole, and front section of a drift tube linac. It can be seamlessly integrated with existing accelerators, achieving significant space and cost savings. Following our beamline, a conventional drift tube linac can further accelerate the beam to the desired energy for specific applications.

Additionally, incorporating the innovative micrometer-sized cooled hydrogen jet plasma method [32,33] holds the promise of generating multiple proton bunches per second. This capability exceeds current limitations and opens exciting avenues for next-generation applications like stereotactic radiosurgery and beyond.

This work investigates the transport of laser-accelerated protons with a wide energy spread through a beamline designed for 109 MeV protons. The protons emerged well-collimated, with a significantly narrowed energy spread of 94.8 ± 3.9 MeV (a reduction from the intended 109 MeV due to passage through the scatterer) and a homogenized beam spot. Additionally, the protons emerged with an 11 mm diameter beam spot while maintaining a transmission efficiency above 2.2%.

The datasets used and/or analyzed during the current study available from the corresponding author on reasonable request.

[1] T. Ziegler, D. Albach, C. Bernert, S. Bock, F.-E. Brack, T. Cowan, N. Dover, M. Garten, L. Gaus, R. Gebhardt *et al.*, Proton beam quality enhancement by spectral phase control of a PW-class laser system, Sci. Rep. **11**, 7338 (2021).

[2] A. Higginson, R. Gray, M. King, R. Dance, S. Williamson, N. Butler, R. Wilson, R. Capdessus, C. Armstrong, J. Green *et al.*, Near-100 mev protons via a laser-driven transparency-enhanced hybrid acceleration scheme, Nat. Commun. **9**, 724 (2018).

[3] N. Zhao, J. Jiao, D. Xie, H. Zhou, S. Zhang, Y. Lang, D. Zou, and H. Zhuo, Near-100 mev proton acceleration from 1021 $\mathrm{w/cm^2}$ laser interacting with near-critical density plasma, High Energy Density Phys. **37**, 100889 (2020).

[4] A. Joulaei and S. Mirzanejhad, Enhanced laser driven ion acceleration by using an AL-DLC double layer target, Optik (Stuttgart) **186**, 120 (2019).

[5] I. Hofmann, J. Meyer-ter-Vehn, X. Yan, A. Orzhekhovskaya, and S. Yaramyshev, Collection and focusing of laser accelerated ion beams for therapy applications, Phys. Rev. ST Accel. Beams **14**, 031304 (2011).

[6] B. Dromey, M. Coughlan, L. Senje, M. Taylor, S. Kuschel, B. Villagomez-Bernabe, R. Stefanuik, G. Nersisyan, L. Stella, J. Kohanoff *et al.*, Picosecond metrology of laser-driven proton bursts, Nat. Commun. **7**, 10642 (2016).

[7] D. Li, T. Yang, M. Wu, Z. Mei, K. Wang, C. Lu, Y. Zhao, W. Ma, K. Zhu, Y. Geng *et al.*, Introduction of research work on laser proton acceleration and its application carried out on compact laser–plasma accelerator at Peking University, Photonics **10**, 132 (2023).

[8] F.-E. Brack, F. Kroll, L. Gaus, C. Bernert, E. Beyreuther, T. E. Cowan, L. Karsch, S. Kraft, L. A. Kunz-Schughart, E. Lessmann *et al.*, Spectral and spatial shaping of laser-driven proton beams using a pulsed high-field magnet beamline, Sci. Rep. **10**, 9118 (2020).

[9] F. Kroll, F.-E. Brack, C. Bernert, S. Bock, E. Bodenstein, K. Brüchner, T. E. Cowan, L. Gaus, R. Gebhardt, U. Helbig *et al.*, Tumour irradiation in mice with a laser-accelerated proton beam, Nat. Phys. **18**, 316 (2022).

[10] P. Chaudhary, G. Milluzzo, H. Ahmed, B. Odlozilik, A. McMurray, K. M. Prise, and M. Borghesi, Radiobiology experiments with ultra-high dose rate laser-driven protons: Methodology and state-of-the-art, Front. Phys. **9**, 624963 (2021).

[11] M. Perry, B. Stuart, G. Tietbohl, J. Miller, J. Britten, R. Boyd, M. Everett, S. Herman, H. Nguyen, H. Powell *et al.*, The petawatt laser and its application to inertial confinement fusion, in *Proceedings of the Summaries of Papers Presented at the Conference on Lasers and Electro-Optics, CLEO-1996, Anaheim, CA* (IEEE, New York, 1996), pp. 307–308.

[12] P. Patel, A. Mackinnon, M. Key, T. Cowan, M. Foord, M. Allen, D. Price, H. Ruhl, P. Springer, and R. Stephens, Isochoric heating of solid-density matter with an ultrafast proton beam, Phys. Rev. Lett. **91**, 125004 (2003).

[13] M. Roth, T. Cowan, M. Key, S. Hatchett, C. Brown, W. Fountain, J. Johnson, D. Pennington, R. Snavely, and S. Wilks *et al.*, Fast ignition by intense laser-accelerated proton beams, Phys. Rev. Lett. **86**, 436 (2001).

[14] M. Würl, C. Gianoli, F. S. Englbrecht, J. Schreiber, and K. Parodi, A Monte Carlo feasibility study on quantitative laser-driven proton radiography, Z. Med. Phys. **32**, 109 (2022).

[15] M. Borghesi, A. Mackinnon, D. H. Campbell, D. Hicks, S. Kar, P. K. Patel, D. Price, L. Romagnani, A. Schiavi, and O. Willi, Multi-mev proton source investigations in ultraintense laser-foil interactions, Phys. Rev. Lett. **92**, 055003 (2004).

[16] J. Cobble, R. Johnson, T. Cowan, N. Renard-Le Galloudec, and M. Allen, High resolution laser-driven proton radiography, J. Appl. Phys. **92**, 1775 (2002).

[17] Y. Li, X. Shen, Y. Yao, S. Wu, A. Pukhov, and B. Qiao, Laser-driven time-limited light-sail acceleration of protons for tumor radiotherapy, Phys. Rev. Res. **5**, 012038 (2023).

[18] L. Pommarel, B. Vauzour, F. Mégnin-Chanet, E. Bayart, O. Delmas, F. Goudjil, C. Nauraye, V. Letellier, F. Pouzoulet, F. Schillaci *et al.*, Spectral and spatial shaping of a laser-produced ion beam for radiation-biology experiments, Phys. Rev. Accel. Beams **20**, 032801 (2017).

[19] F. Romano, F. Schillaci, G. Cirrone, G. Cuttone, V. Scuderi, L. Allegra, A. Amato, A. Amico, G. Candiano, G. De Luca *et al.*, The elimed transport and dosimetry beamline for laser-driven ion beams, Nucl. Instrum. Methods Phys. Res., Sect. A **829**, 153 (2016).

[20] U. Masood, M. Bussmann, T. Cowan, W. Enghardt, L. Karsch, F. Kroll, U. Schramm, and J. Pawelke, A compact solution for ion beam therapy with laser accelerated protons, Appl. Phys. B **117**, 41 (2014).

[21] I. Hofmann, J. Meyer-ter-Vehn, X. Yan, and H. Al-Omari, Chromatic energy filter and characterization of laser-accelerated proton beams for particle therapy, Nucl. Instrum. Methods Phys. Res., Sect. A **681**, 44 (2012).

[22] W. Wang, Y. Yin, D. Zou, T. Yu, H. Xu, and F. Shao, Effects of parameters on the proton focusing driven by coulomb explosion, High Energy Density Phys. **32**, 77 (2019).

[23] J. Domański and J. Badziak, Ultra-intense femtosecond super-heavy ion beams driven by a multi-PW laser, Phys. Lett. A **382**, 3412 (2018).

[24] B. Albertazzi, A. Ciardi, M. Nakatsutsumi, T. Vinci, J. Béard, R. Bonito, J. Billette, M. Borghesi, Z. Burkley, S. Chen *et al.*, Laboratory formation of a scaled protostellar jet by coaligned poloidal magnetic field, Science **346**, 325 (2014).

[25] H. Daido, M. Nishiuchi, and A. S. Pirozhkov, Review of laser-driven ion sources and their applications, Rep. Prog. Phys. **75**, 056401 (2012).

[26] F. Wagner, O. Deppert, C. Brabetz, P. Fiala, A. Kleinschmidt, P. Poth, V. Schanz, A. Tebartz, B. Zielbauer, M. Roth *et al.*, Maximum proton energy above 85 mev from the relativistic interaction of laser pulses with micrometer thick CH_2 targets, Phys. Rev. Lett. **116**, 205002 (2016).

[27] G. Petrov, C. McGuffey, A. Thomas, k. Krushelnick, and F. Beg, Generation of heavy ion beams using femtosecond laser pulses in the target normal sheath acceleration and radiation pressure acceleration regimes, Phys. Plasmas **23**, 063108 (2016).

[28] Z. Z. Nezam, A. Ghasemizad, and S. Khoshbinfar, A hybrid simulation of carbon ion beams generation, acceleration and the evaluation of the ignition condition, Nucl. Instrum. Methods Phys. Res., Sect. A **969**, 164050 (2020).

[29] J. Braenzel, A. Andreev, K. Platonov, M. Klingsporn, L. Ehrentraut, W. Sandner, and M. Schnürer, Coulomb-driven energy boost of heavy ions for laser-plasma acceleration, Phys. Rev. Lett. **114**, 124801 (2015).

[30] H. Al-Omari, I. Hofmann, V. Bagnoud, S. Busold, C. Brabetz, D. Schumacher, A. Almomani, M. Roth, and O. Deppert, Space-charge effect of laser accelerated protons on beam profile and permanent magnet quadrupole focal line, Nucl. Instrum. Methods Phys. Res., Sect. A **981**, 164523 (2020).

[31] S. Weng, Z. Sheng, M. Murakami, M. Chen, M. Liu, H. Wang, T. Yuan, and J. Zhang, Optimization of hole-boring radiation pressure acceleration of ion beams for fusion ignition, Matter Radiat. Extremes **3**, 28 (2018).

[32] M. Rehwald, S. Assenbaum, C. Bernert, F.-E. Brack, M. Bussmann, T. E. Cowan, C. B. Curry, F. Fiuza, M. Garten, L. Gaus *et al.*, Ultra-short pulse laser acceleration of protons to 80 mev from cryogenic hydrogen jets tailored to near-critical density, Nat. Commun. **14**, 4009 (2023).

[33] Helmholtz Association of German Research Centres, New Method Improves Proton Acceleration with High Power Laser Using Frozen Hydrogen as Target, https://phys.org/news/2023-07-method-proton-high-power-laser.html.

[34] A. Almomani, M. Droba, U. Ratzinger, and I. Hofmann, Matching the laser generated p bunch into a crossbar-h drift tube linac, Phys. Rev. ST Accel. Beams **15**, 051302 (2012).

[35] D. Margarone, G. P. Cirrone, G. Cuttone, A. Amico, l. Andò, M. Borghesi, S. S. Bulanov, S. V. Bulanov, D. Chatain, A. Fajstavr *et al.*, Elimaia: A laser-driven ion accelerator for multidisciplinary applications, Quantum Beam Sci. **2**, 8 (2018).

[36] F. Schillaci, L. Pommarel, F. Romano, G. Cuttone, M. Costa, D. Giove, M. Maggiore, A. Russo, V. Scuderi, V. Malka *et al.*, Characterization of the elimed permanent magnets quadrupole system prototype with laser-driven proton beams, J. Instrum. **11**, T07005 (2016).

[37] M. Scisciò, M. Migliorati, L. Palumbo, and P. Antici, Design and optimization of a compact laser-driven proton beamline, Sci. Rep. **8**, 6299 (2018).

[38] S. Busold, D. Schumacher, O. Deppert, C. Brabetz, S. Frydrych, F. Kroll, M. Joost, H. Al-Omari, A. Blažević, B. Zielbauer *et al.*, Focusing and transport of high-intensity multi-mev proton bunches from a compact laser-driven source, Phys. Rev. ST Accel. Beams **16**, 101302 (2013).

[39] S. Busold, D. Schumacher, C. Brabetz, D. Jahn, F. Kroll, O. Deppert, U. Schramm, T. E. Cowan, A. Blažević, V. Bagnoud *et al.*, Towards highest peak intensities for ultra-short mev-range ion bunches, Sci. Rep. **5**, 12459 (2015).

[40] D. Jahn, D. Schumacher, C. Brabetz, F. Kroll, F. Brack, J. Ding, R. Leonhardt, I. Semmler, A. Blažević, U. Schramm *et al.*, Focusing of multi-mev, subnanosecond proton bunches from a laser-driven source, Phys. Rev. Accel. Beams **22**, 011301 (2019).

[41] I. Hofmann, Performance of solenoids versus quadrupoles in focusing and energy selection of laser accelerated protons, Phys. Rev. ST Accel. Beams **16**, 041302 (2013).

[42] D. Uriot and N. Pichoff, TraceWin, CEA Saclay 596, 2014.

[43] J. Ziegler, J. Biersack, M. Ziegler, D. Marwick, and G. Cuomo, SRIM-2013 code, IBM Company, 2013.

[44] J. Zhu, M. Wu, K. Zhu, Y. Geng, Q. Liao, D. Li, T. Yang, M. Easton, C. Li, X. Xu *et al.*, Demonstration of tailored energy deposition in a laser proton accelerator, Phys. Rev. Accel. Beams **23**, 121304 (2020).

[45] J. Fan, W. Luo, E. Fourkal, T. Lin, J. Li, I. Veltchev, and C. Ma, Shielding design for a laser-accelerated proton therapy system, Phys. Med. Biol. **52**, 3913 (2007).

[46] U. Masood, T. Cowan, W. Enghardt, K. Hofmann, L. Karsch, F. Kroll, U. Schramm, J. Wilkens, and J. Pawelke, A light-weight compact proton gantry design with a novel dose delivery system for broad-energetic laser-accelerated beams, Phys. Med. Biol. **62**, 5531 (2017).

[47] J. Zhu, M. Wu, Q. Liao, Y. Geng, K. Zhu, C. Li, X. Xu, D. Li, Y. Shou, T. Yang *et al.*, Experimental demonstration of a laser proton accelerator with accurate beam control through image-relaying transport, Phys. Rev. Accel. Beams **22**, 061302 (2019).

[48] K. Wang, K. Zhu, M. J. Easton, Y. Li, C. Lin, and X. Yan, Achromatic beamline design for a laser-driven proton therapy accelerator, Phys. Rev. Accel. Beams **23**, 111302 (2020).

[49] F. Li, Y. Yan, Q. Wang, Y. Xia, K. Wang, Z. Guo, Y. Wang, K. Chen, E. Guo, K. Zhu *et al.*, Real-time beam transport simulator for wide energy-spread proton beam generated by laser acceleration, Phys. Rev. Accel. Beams **26**, 114601 (2023).

[50] P. Mora, Plasma expansion into a vacuum, Phys. Rev. Lett. **90**, 185002 (2003).

[51] Atomic interaction with matter (ATIMA) code, https://www.isotopea.com/webatima/.